

# Maximum compatibility estimates and shape reconstruction with boundary curves and volumes of generalized projections

Mikko Kaasalainen  
 Department of Mathematics  
 Tampere University of Technology  
 P.O. Box 553, 33101 Tampere  
 Finland

## Abstract

We show that the boundary curves (profiles) in  $\mathbb{R}^2$  of the generalized projections of a body in  $\mathbb{R}^3$  uniquely determine a large class of shapes, and that sparse profile data, combined with projection volume (brightness) data, can be used to reconstruct the shape and the spin state of a body. We also present an optimal strategy for the relative weighting of the data modes in the inverse problem, and derive the maximum compatibility estimate (MCE) that corresponds to the maximum likelihood or maximum a posteriori estimates in the case of a single data mode. MCE is not explicitly dependent on the noise levels, scale factors or numbers of data points of the complementary data modes, and can be determined without the mode weight parameters. We present a solution method well suitable for adaptive optics images in particular, and discuss various choices of regularization functions.

AMS subject classifications: 68U05, 65D18, 52B10, 49N45, 65J22, 85-08

Keywords: Computational geometry, three-dimensional polytopes, inverse problems, computational methods in astronomy

## 1 Introduction

Constructing the shape model of a three-dimensional object or a surface is often based on images obtained at various viewing geometries. This is the standard case in human and robot vision as well as in cartography. When individual points on the surface can be identified in different images, one can directly solve for their position vectors and use this as a top-down basis for stereographic mapping or model construction. In many cases, however, the model construction reduces to an inverse problem rather than a cartographic one as the image information is based purely on the projections of the target in the viewing directions. When surface illumination and other effects are taken into account, we talk about *generalized projections* [14] to distinguish these from simple shadow-like projections or silhouettes. As discussed in [14], there are various types of such projections, ranging from the volume-like quantity of integrated brightness  $L \in \mathbb{R}$  (generalization of the area of a shadow on a projection screen) to resolved images  $\mathcal{I} \in \mathbb{R}^2 \times \mathbb{R}$  (for one wavelength).

In this paper, we consider the case where images  $\mathcal{I}(\omega, \omega_0)$  obtained at various viewing and illumination directions  $\omega, \omega_0 \in S^2$  are available, but the information in these images is only contained in the boundary curves between the dark background or a shadow and the illuminated portion of the target surface. This situation is typical for faraway objects in space for which low-resolution images are available via large telescopes through adaptive optics (AO) [19] or other deconvolution and image processing techniques. Due to the deconvolution process, the actual brightness levels of the pixels in these images tend to portray artificial and exaggerated features, so they are usually less reliable than profile contours, i.e., the locations of the light/dark boundary pixels [2, 3].

As the coverage of viewing geometries is seldom wide enough to enable a full reconstruction of the model from images alone, we also consider the possibility of augmenting the image dataset with a set of measured brightnesses  $L(\omega, \omega_0)$  of the target at various observing geometries. Subsets of these, measured within some time intervals, are called lightcurves. As discussed in [10]-[14] (see also references therein), a global, usually convex, model of the target can be obtained from a large enough set of  $L(\omega, \omega_0)$ . The possibility to use images  $\mathcal{I}$  both serves to reconstruct more details in the model and to use a combined dataset for successful modelling when neither the available  $L$  nor  $\mathcal{I}$  are sufficient alone.

The ratio of profile contour pixels to all pixels of the target is approximately  $4/D$ , where  $D$  is a typical diameter of the target in pixels. For the largest few asteroid AO targets,  $D$  is around 30. When  $D$  is less than about 10, the location accuracy of the border pixels is not necessarily very much better than the brightness accuracy of the pixels, but on the other hand there is no particular loss in the number of information points when only borders are used. For higher  $D$ , border points are a smaller subset of available pixels, but now their location accuracy is far better than the brightness accuracy of all pixels [2, 3].

The profile contours of the AO images are obtained as a solution of a separate inverse (or imaging) problem, where an approximation of the atmospheric point-spread function (PSF) is first used to deconvolve the raw image (with, e.g., connectedness of the processed image as a constraint), and the contours can be separately modelled with wavelet techniques [2, 3, 19]. This independence from the actual model of the target is advantageous in the sense that the assumptions and inevitable deficiencies of the model (particularly in the adopted light-scattering model on the surface [15]) do not affect the outcome of the AO image processing. On the other hand, from the methodological point of view, all information should usually be employed simultaneously when solving an inverse problem, so another approach would be to use the raw AO image data and the approximated PSF directly in model construction without separate image deconvolution. However, in practice it appears that the profile curve extraction procedure, in particular, retains valuable independent information [2, 3], and the model deficiencies affect the fit deviation between the predicted and observed model profile curves less than they affect that between the full model and AO images. What is more, below we show that the profile curves convey almost as much information on the shape as the full images, so we can conclude that the two-step inversion of AO (and brightness) data is well justified.

The paper is organized in sections in the following manner. In Section 2 we study the information content of profile contours and show uniqueness results for the inverse problem of reconstructing shapes from these. Section 3 deals with the posing of the inverse problem and the choice of regularization functions. In Section 4, we discuss the weighting and maximum compatibility estimates for inverse problems with multiple data modes, and examples of the use of real brightness data  $L$  and images  $\mathcal{I}$  are presented in Section 5. Section 6 sums up.

## 2 Generalized profiles: uniqueness results

In this section, we define the concept of generalized profiles as boundary curves corresponding to generalized projections, and show that a large class of shapes is reconstructable from these. While many practical procedures for shape-from-profiles (also known as volume carving) and shape-from-shading are well known in, e.g., computer vision (see [21] and references therein) and cartography (clinometry), some of their geometric characteristics and the properties of the corresponding shape classes and inverse problems discussed here have not been previously stated in the mathematical literature, to the best of our knowledge.

Let us first look at classical profiles defined by one direction  $\omega \in S^2$ , i.e.,  $\omega_0 = \omega$ . The projection  $\mathcal{P}(\omega, \mathcal{B}) \in \mathbb{R}^2$  of a compact set  $\mathcal{B} \in \mathbb{R}^3$  (a set of points on closed surfaces) in the direction  $\omega \in S^2$  maps  $x \in \mathcal{B} \rightarrow \varkappa \in \mathcal{P}$ :

$$\varkappa = \begin{pmatrix} 0 & 1 & 0 \\ 0 & 0 & 1 \end{pmatrix} R_y(\vartheta - \frac{\pi}{2}) R_z(\psi) x, \quad (1)$$

where  $0 < \vartheta < \pi, 0 \leq \psi < 2\pi$  are the polar coordinate angles defining

$$\omega = (\sin \vartheta \cos \psi, \sin \vartheta \sin \psi, \cos \vartheta),$$

and  $R_i(\alpha)$  is the rotation matrix corresponding to the rotation of the coordinate frame through angle  $\alpha$  in the positive direction about the  $i$ -axis. Thus, e.g.,  $R_z(\phi)$  is

$$R_z(\phi) = \begin{pmatrix} \cos \phi & \sin \phi & 0 \\ -\sin \phi & \cos \phi & 0 \\ 0 & 0 & 1 \end{pmatrix}. \quad (2)$$

For  $\vartheta = 0$ ,  $\varkappa_i = x_i, i = 1, 2$ , and for  $\vartheta = \pi$ ,  $\varkappa_1 = -x_1, \varkappa_2 = x_2$ . Only a half of  $S^2$  is needed for defining  $\omega$  as

$$\varkappa_i(\omega) = (-1)^i \varkappa_i(-\omega).$$

For some definitions below, we need to give the three-dimensional position  $x_{\varkappa}(\omega) \in \mathbb{R}^3$  of the planar points  $\varkappa$ :

$$x_{\varkappa}(\omega) = R_z(-\psi)R_y\left(\frac{\pi}{2} - \vartheta\right) \begin{pmatrix} 0 \\ \varkappa_1 \\ \varkappa_2 \end{pmatrix}. \quad (3)$$

**Definition 1.** The *profile*  $\mathcal{P}_{\partial}(\omega, \mathcal{B})$  of  $\mathcal{B}$  in the direction  $\omega$  is the boundary of its projection  $\mathcal{P}(\omega, \mathcal{B})$ :

$$\mathcal{P}_{\partial}(\omega, \mathcal{B}) = \partial\mathcal{P}(\omega, \mathcal{B})$$

(the specific notation  $\mathcal{P}_{\partial}$  is used for emphasis). More specifically,  $\mathcal{P}_{\partial}(\omega, \mathcal{B})$  is the mapping  $x \rightarrow \varkappa$  from those points  $x \in \mathcal{B}$  for which, for all lines  $x + s\omega$  parametrized by  $s$ ,

$$\mathcal{P}_{\partial}(\omega, \mathcal{B}) = \left\{ \varkappa \mid \forall s : \exists \theta, \exists \rho > 0 : \mathfrak{P}(x + s\omega; \theta, \rho) \notin \mathcal{B}, 0 < \rho < \rho \right\}, \quad (4)$$

where  $\mathfrak{P}(\mathcal{L}; \theta, \rho)$  denotes a parallel transport, perpendicular to the line  $\mathcal{L}$ , of  $\mathcal{L}$  by the amount  $\rho$  in the direction  $\theta \in S^1$  in some system around  $\mathcal{L}$ .

**Definition 2.** The *cylinder continuation* (CC)  $\mathcal{C}(\omega, \mathcal{S})$  of a set  $\mathcal{S}$  of points  $x \in \mathbb{R}^3$  is the set of points in  $\mathbb{R}^3$  given by

$$\mathcal{C}(\omega, \mathcal{S}) = \left\{ x + s\omega \mid x \in \mathcal{S}; -\infty < s < \infty \right\}. \quad (5)$$

**Definition 3.** The *profile hull*  $\mathcal{H} \in \mathbb{R}^3$  is the bounding surface of the set of points formed by the intersection of the CCs of the projections  $\mathcal{P}$  in some directions  $\omega_i, i = 1, \dots, N$ , corresponding to measured profiles  $\mathcal{P}_{\partial}(\omega_i) \in \mathbb{R}^2$ :

$$\mathcal{H}(\{\mathcal{P}_{\partial}(\omega_i)\}_{i=1}^N) = \partial \bigcap_i \mathcal{C}(\omega_i, \mathcal{S}_i), \quad \mathcal{S}_i = \left\{ x_{\varkappa}(\omega_i) \mid \varkappa \in \mathcal{P}(\omega_i) \right\}. \quad (6)$$

**Remark.** For practical purposes and clarity, we assume  $\mathcal{H}$  to be constructed such that it has a closed surface as a boundary, though this is not strictly necessary in its definition (we could define  $\mathcal{H}$  as set of points rather than its bounding surface). Thus  $\mathcal{B}$  and  $\mathcal{H}$  are in the same object class. Similarly, we use the concepts of projection and profile (or body and surface) somewhat interchangeably when the meaning is obvious.

Many bodies can be reconstructed to arbitrary accuracy with profile hulls. A convex body is already determined by its  $\mathcal{H}$  constructed with a full coverage of the directions  $\omega$  confined to any plane in  $\mathbb{R}^3$ . In real profile measurements, however, the position of the profile in the  $\varkappa$ -plane is usually arbitrary, i.e., the profile is determined up to a translation  $\varkappa_0$  of the profile plane origin. Then data restricted to planar directions are not necessarily sufficient even for convex bodies: the profile offsets  $\varkappa_{0,i}$  of a convex body are not always uniquely defined by the profiles  $\mathcal{P}_{\partial}(\omega_i)$  via the profile hull  $\mathcal{H}$  when  $\omega_i$  are confined to a

plane. This is simple to illustrate by considering curves in  $\mathbb{R}^2$  and their projections in  $\mathbb{R}$  at directions in  $S^1$ .

If the curvature function  $C : S^1 \rightarrow \mathbb{R}$  of a closed convex curve in  $\mathbb{R}^2$  is given by a real-valued non-negative Fourier series

$$C(\varphi) = \Re \sum_n c_n e^{in\varphi} \geq 0, \quad n \geq 0,$$

where  $\varphi$  denotes the direction of the outward normal of the curve, the projected width  $w(\varphi)$  of the contour in that direction is

$$w(\varphi) = \int_{-\pi/2}^{\pi/2} C(\psi + \varphi) \cos \psi \, d\psi = \Re \sum_n c_n e^{in\varphi} I_n,$$

where

$$I_n = \int_{-\pi/2}^{\pi/2} \cos n\psi \cos \psi \, d\psi$$

and for  $n \neq 1$

$$I_n = \begin{cases} 0 & n = 3, 5, 7, \dots \\ 2/(n^2 - 1) & n = 2, 6, 10, \dots \\ 2/(1 - n^2) & n = 0, 4, 8, \dots \end{cases}$$

and  $c_1 \equiv 0$  since  $I_1 \neq 0$  and we must have  $w(\varphi) = w(\varphi + \pi)$ . Thus  $w(\varphi)$  carries no information on the odd-valued  $n$ -coefficients of the curvature function  $C(\varphi)$  that uniquely defines the shape of the curve (cf. [10] for convex surfaces in  $\mathbb{R}^3$ ). Thus, for cylindrical convex surfaces in  $\mathbb{R}^3$ , the observed profiles in the symmetry plane can be made to correspond to any odd parts of  $C(\varphi)$  with suitable chosen offsets  $\varkappa_0$ . A typical case is that of shapes mimicking a circular cylinder with constant  $C$  in the symmetry plane: for example, if we change  $\varkappa_0 = 0$  to

$$\varkappa_0^{(1)}(\varphi) = R(-1)^\varphi \operatorname{div}^{\frac{\pi}{3}} \left[ \frac{2}{\sqrt{3}} \cos(\varphi \bmod \frac{\pi}{3} - \frac{\pi}{6}) - 1 \right], \quad (7)$$

the reconstructed shape is a cylindrical Reuleaux triangle. This degeneracy occurs since for projections  $\mathbb{R}^2 \rightarrow \mathbb{R}$  the volume of a profile is equivalent to the profile itself up to an offset. An additional profile from a direction perpendicular to the plane resolves the degeneracy.

Thus, in general, we need data at full  $\omega \in S^2$  for a unique reconstruction of a body when the profile offsets are not known. The principle in the reconstruction via the profile hull  $\mathcal{H}$  is the requirement that  $\mathcal{H}$  must be consistent with the observed profiles, i.e., the profiles of the constructed  $\mathcal{H}$  must be identical to the observed ones:

$$\mathcal{P}_\partial[\omega_i, \mathcal{H}(\{\mathcal{P}_\partial(\omega_j)|_{j=1}^N\})] = \mathcal{P}_\partial(\omega_i)$$

(otherwise the volume of the intersection defining  $\mathcal{H}$  is not maximal).

Let us denote by the *complete profile hull*  $\mathcal{H}_C$  the profile hull for which  $\omega$  covers all of  $S^2$ . The complete profile hull  $\mathcal{H}_C(\mathcal{B})$  of a body  $\mathcal{B}$  is the envelope of those of its tangents that do not intersect  $\mathcal{B}$  anywhere. Then we can define a class of surfaces that includes convex ones but extends far into nonconvex surfaces:

**Definition 4.** *Tangent-covered bodies* (TCBs) are bodies that are their own complete profile hulls:  $\mathcal{B} = \mathcal{H}_C(\mathcal{B})$ . Thus, each surface point  $x \in \mathcal{B}$  of a TCB is mapped at least to one  $\mathcal{P}_\partial(\omega)$ .

TCBs include a large variety of nonconvex surfaces or sets of them: for example, a body consisting of two separate spheres is a TCB. While convex bodies  $\mathcal{C}$  are reconstructable from the volumes of their generalized projections [10, 14] and are defined by having no tangents intersecting the body, TCBs  $\mathcal{T}$  are reconstructable from profiles and are defined by there being at least one tangent at each surface point not intersecting the body elsewhere.

Let us now generalize the concept of profile in the same way as projections. This leads to a shape class  $\mathcal{G}$ , larger than TCBs  $\mathcal{T}$ , that can be reconstructed from generalized profiles:

$$\mathcal{C} \subset \mathcal{T} \subset \mathcal{G}.$$

When we consider the directions  $(\omega, \omega_0)$  in  $S^2 \times S^2$ , the region both visible and illuminated on  $\mathcal{B}$  is given by [14, 11]

$$\mathcal{A}_+(\omega, \omega_0; \mathcal{B}) = \mathcal{A}_+(\omega; \mathcal{B}) \cap \mathcal{A}_+(\omega_0; \mathcal{B}), \quad (8)$$

where

$$\mathcal{A}_+(\omega; \mathcal{B}) = \left\{ x \in \mathcal{B} \mid \langle \nu(x), \omega \rangle \geq 0; \forall s > 0 : x + s\omega \notin \mathcal{B} \right\}, \quad (9)$$

where  $\nu(x)$  is the unit surface normal at  $x$ . The projection  $\mathcal{P}$  of the boundary  $\partial\mathcal{A}_+$  is now the generalized profile:

**Definition 5.** The *generalized profile* of the body  $\mathcal{B}$  in the direction  $\omega$  and at illumination direction  $\omega_0$  is

$$\partial\mathcal{P}[\omega, \mathcal{A}_+(\omega, \omega_0; \mathcal{B})] = \mathcal{P}[\omega, \partial\mathcal{A}_+(\omega, \omega_0; \mathcal{B})]. \quad (10)$$

The shape class  $\mathcal{G}$  is not as straightforward to define as  $\mathcal{C}$  and  $\mathcal{T}$ . We can, however, prove configurations allowing unique shape determination that illustrate its extension from  $\mathcal{T}$ .

**Theorem 1.** *Assume that we know some parts  $\mathcal{K}$  of a body  $\mathcal{B}$  from profile measurements. There exist configurations in which unknown parts  $\mathcal{U}$  of  $\mathcal{B}$  not determinable from profiles can be uniquely determined from the generalized profiles of  $\mathcal{B}$  by using the shadow boundaries of  $\mathcal{K}$  on  $\mathcal{U}$ .*

*Proof.* Assume that  $\mathcal{H}_C(\mathcal{B})$  is defined, and that it contains a planar section  $\mathcal{K}$ , and that  $\mathcal{B}$  contains in this region an unknown concavity  $\mathcal{U}$  (corresponding to  $\mathcal{H}_C \setminus \mathcal{B}$ ). Also, assume that all points of  $\mathcal{U}$  are seen from the viewing direction  $\omega \perp \mathcal{K}$ , and that the illumination direction  $\omega_0$  lies in a plane  $\perp \mathcal{K}$ , with  $\theta = \angle(\omega_0, \mathcal{K})$ . Then the planar edge curve of the concavity  $\mathcal{U}$  can be determined when  $\theta \rightarrow 0$ :

$$\partial\mathcal{U} = \lim_{\theta \rightarrow 0} \partial S(\theta) := \partial S_0,$$

where  $\partial S$  denotes the projection of the shadow boundary in the direction  $\omega$  on the plane  $\mathcal{K}$ . At various  $0 < \theta \leq \pi/2$ , we can measure the shadow boundary projections  $\partial S(\theta)$ , and thus extract the projection  $\partial\tilde{S}(\theta)$  of the shadow boundary inside  $\mathcal{U}$ :

$$\partial\tilde{S}(\theta) = \partial S(\theta) \setminus \partial\hat{S}(\theta), \quad \partial\hat{S}(\theta) := \partial S(\theta) \cap \partial S_0.$$

Then the envelope in  $\mathbb{R}^3$  of the intersection curves of the cylinder continuations of  $\partial\tilde{S}(\theta)$  in the directions of  $\omega$  and  $\omega_0$

$$\mathcal{C}[\omega, \partial\tilde{S}(\theta)] \cap \mathcal{C}[\omega_0, \partial\hat{S}(\theta)]$$

uniquely constructs the surface of the concavity  $\mathcal{U}$  (when  $\mathcal{U}$  is suitably regular).  $\square$

**Theorem 2.** *There exist configurations in which unknown parts  $\mathcal{U}$  of  $\mathcal{B}$  can be uniquely determined by using their shadow boundaries on the known part  $\mathcal{K}$ .*

*Proof.* Let  $\mathcal{B}$  be a combination of a TCB  $\mathcal{E}$  and any surface  $\mathcal{D}$  ( $\mathcal{E} \cap \mathcal{D} = \emptyset$ ) that can be determined using profiles in the directions  $\omega$  for which the profile intersection

$$\mathcal{Q}(\omega) := \mathcal{P}(\omega, \mathcal{D}) \cap \mathcal{P}(\omega, \mathcal{E})$$

vanishes,  $\mathcal{Q} = \emptyset$  (the whole of  $\mathcal{D}$  is in the known part  $\mathcal{K}$ ). The unknown parts are assumed to be on  $\mathcal{E}$  (they cannot be determined using the above  $\omega$ ). Now the parts of profiles of  $\mathcal{E}$  that merge with  $\mathcal{P}(\omega, \mathcal{D})$  at some  $\omega$ , i.e.,  $\mathcal{Q}(\omega) \neq \emptyset$ , are represented as shadows on  $\mathcal{D}$  that we assume we can see from some directions  $\omega'$ . The full or partial profiles of  $\partial\mathcal{P}(\omega, \mathcal{E})$  for which  $\partial\mathcal{P}(\omega, \mathcal{E}) \cap \mathcal{Q} = \emptyset$  can be determined as usual, and, with a known  $\mathcal{D}$ , the remaining parts  $\partial\mathcal{P}(\omega, \mathcal{E}) \cap \mathcal{Q} \neq \emptyset$  can be determined from the shadows on  $\mathcal{D}$ . The intersection

$$\partial\mathcal{W} = \mathcal{C}[\omega', \partial S_p(\omega')] \cap \mathcal{D},$$

where  $\mathcal{C}[\omega', \partial S_p(\omega')]$  denotes the cylinder continuation corresponding to the observed projection of the shadow boundary of  $\mathcal{E}$  on  $\mathcal{D}$  in the direction  $\omega'$ , can be used to determine the projection  $\mathcal{P}(\partial\mathcal{W}, \omega)$ , which completes the missing parts of the needed profiles. Now we have constructed the set of full profiles of  $\mathcal{E}$  at all  $\omega \in S^2$ , so  $\mathcal{E}$  can be constructed as it is a TCB.  $\square$

Continuing in a similar manner, we can construct more complex variations of the two cases above to explore the shape class  $\mathcal{G}$ . In practice, directions  $(\omega, \omega_0)$  seldom cover  $S^2 \times S^2$  extensively or densely, so the shape is reconstructed within some resolution (discretization degree of the model) and a priori assumptions, as discussed below.

### 3 Inverse problem

Let us now consider the inverse problem of determining the shape and spin state of a body  $\mathcal{B}$  from some measured generalized profiles  $\partial\mathcal{P}[\omega_i, \mathcal{A}_+(\omega_i, \omega_{0i}; \mathcal{B})]$  and the volumes  $L(\omega_{0i}, \omega_i)$  of generalized projections. We present a method that is suitable for typical ground-based astronomical data, i.e., the profiles are only obtained at restricted geometries and their resolution level is not high. When a dense coverage of geometries and high resolution are available (e.g., space probe missions), direct methods of computer vision and cartography are usually applicable.

Our goal is to construct a total goodness-of-fit measure  $\chi_{\text{tot}}^2$

$$\chi_{\text{tot}}^2 = \chi_L^2 + \lambda_{\partial}\chi_{\partial}^2 + \lambda_R g(P), \quad (11)$$

where  $L$  denotes lightcurves,  $\partial$  generalized profiles, and  $R$  regularizing functions  $g(P)$ , where  $P \in \mathbb{R}^p$  is the vector of model parameters. Regularization is discussed at the end of this section, and the determination of the weights  $\lambda$  in section 4. We note here that the additional  $g(P)$  make  $\chi_{\text{tot}}^2$  pseudo- $\chi^2$  as it no longer describes an underlying (assumed) Gaussian probability distribution (though  $g(P)$  may be  $\chi^2$ -like in their functional form). When probability densities such as a posteriori distributions are constructed from  $\chi_{\text{tot}}^2$ , one can assume  $\chi^2$ -distributions (of the form  $e^{-c\chi^2}$ ) only for the data components, and other suitable (prior) distributions for the regularization components [17] such that the maximum of the a posteriori distribution occurs at  $\arg \min \chi_{\text{tot}}^2(P)$ .

Throughout this paper, we do not include the conventional  $1/\delta^2$ -factor in  $\chi^2$ -forms, where  $\delta$  is the expected (Gaussian) error variance (noise level), since  $\delta$  is seldom known exactly, and it does not affect the determination of our point estimates which is the goal of this paper. Suitable parameters for Gaussian or other distribution widths can be inserted separately whenever we want to construct a distribution.

The volumes of generalized projections are also called total or disk-integrated brightnesses [10, 11, 14]:

$$L(\omega_0, \omega) = \int_{\mathcal{A}_+} R(x; \omega_0, \omega) \langle \omega, \nu(x) \rangle d\sigma(x) \equiv \int_{\mathcal{P}(\omega, \mathcal{A}_+)} R[P^{-1}(\omega, \mathcal{A}_+, \varkappa); \omega_0, \omega] d^2\varkappa, \quad (12)$$

where  $\nu(x)$  and  $d\sigma(x)$  are, respectively, the outward surface normal and surface patch of  $\mathcal{B}$ ,  $R(x; \omega_0, \omega)$  describes the intensity of scattered light at the point  $x$  on the surface,  $P^{-1}(\omega, \mathcal{A}_+, \varkappa)$  is the point in  $\mathcal{A}_+$  corresponding to the projection point  $\varkappa$ , and  $d^2\varkappa$  is the surface patch of the projection  $\mathcal{P}$ . In its basic form,

$$\chi_L^2 = \sum_i [L^{(\text{obs})}(\omega_{0i}, \omega_i) - L^{(\text{mod})}(\omega_{0i}, \omega_i)]^2 \quad (13)$$

(assuming a constant noise level; see [11] for modifications and variations of this).  $L$ -data on  $S^2 \times S^2$  uniquely determine a convex body and the solution is stable [10, 14], but  $L$ -data do not carry information on nonconvexities in most realistically available  $S^2 \times S^2$  geometries in practice [6]. Such information must be provided by AO or other techniques.

For many typical AO targets, the generalized profiles are starlike due to the proximity of  $\omega$  and  $\omega_0$  and some regularity of the target shape at global scale [2, 3, 19]. Then we can write  $\chi_{\partial}^2$  by considering, for each profile  $i$ , their observed and modelled maximal radii (from some point within the profile) on the projection plane  $\varkappa = (\xi, \eta) \in \mathbb{R}^2$  at direction angles  $\alpha_{ij}$  (starting from a chosen coordinate direction for positive  $\xi$ ,  $\eta = 0$ ):

$$\chi_{\partial}^2 = \sum_{ij} [r_{\text{max}}^{(\text{obs})}(\alpha_{ij}) - r_{\text{max}}^{(\text{mod})}(\alpha_{ij})]^2. \quad (14)$$

As the accuracy of  $r_{\max}^{(\text{obs})}$  is proportional to the size of the image, the sum (14) automatically takes this weighting into account (of course, direct weighting due to varying noise levels can be used as well).

We now represent the body  $\mathcal{B}$  as a polytope [11]. Let two vertices  $a$  and  $b$  of a facet have projection points  $(\xi_a, \eta_a)$ ,  $(\xi_b, \eta_b)$ , and  $(\xi_0, \eta_0)$  be the point on the projection plane from which the radii and  $\alpha$  are measured (this defines the profile offset that must be solved for in the inverse problem). With

$$\begin{aligned} A &= -\sin \alpha, & B &= \cos \alpha, \\ C &= \eta_a - \eta_b, & D &= \xi_b - \xi_a, \\ E &= A\xi_0 + B\eta_0, & F &= \xi_b\eta_a - \xi_a\eta_b, \end{aligned} \quad (15)$$

the intersection point of the radius line and the projection of the facet edge  $ab$  is at

$$\xi = \frac{DE - BF}{AD - BC}, \quad \eta = \frac{AF - CE}{AD - BC}, \quad (16)$$

and, to be in the correct direction of  $\alpha$  and between the points  $a$  and  $b$ , the intersection point must satisfy

$$\begin{aligned} (\xi - \xi_a)(\xi_b - \xi) &\geq 0, & (\xi - \xi_0) \cos \alpha &\geq 0, \\ (\eta - \eta_a)(\eta_b - \eta) &\geq 0, & (\eta - \eta_0) \sin \alpha &\geq 0. \end{aligned} \quad (17)$$

If  $AD - BC = 0$ , the line in  $\alpha$ -direction is parallel to the line  $ab$ , so there is no intersection unless the lines coincide, i.e., either of the numerators in (16) vanishes.

The model  $r_{\max}(\alpha)$  can now be determined by going through all eligible facet edges and their intersection points  $\varkappa_{ab}(\alpha)$ :

$$r_{\max}^{(\text{mod})}(\alpha) = \max \left\{ \|\varkappa_{ab}(\alpha) - \varkappa_0\| \mid a, b \in \mathcal{V}_+ \right\}, \quad (18)$$

where  $\mathcal{V}_+$  is the set of vertices of the facets  $\mathcal{A}_+$  that are both visible and illuminated. The set  $\mathcal{A}_+$  of (9) is determined by ray-tracing [12]. It is an approximation (correct to the order of the average facet area) of the actual visible and illuminated region, i.e., each facet either is or is not in  $\mathcal{A}_+$  (judging by its centroid): projection lines of obstructing facets inside a facet are neglected when the facets are small enough.

The principle of using outer contours applies to AO data that do not generally show non-starlike or multiple contours (due to crater shadows) as the solar phase angles  $\arccos(\omega, \omega_0)$  are low and the resolution/deconvolution accuracy is not high. At high phase angles, even starlike bodies form non-starlike contours, and contours inside the outer contour appear in high-resolution images from probe flybys.

The outer contour  $\partial\mathcal{O}$  can be automatically derived for non-starlike shape models as well; such models can be constructed by, e.g., joining starlike submodels together, using a cylindrical coordinate frame [11], or by determining the coordinates of a set of points with which a suitable surface (a new tessellation for each iteration) is defined via, e.g., mesh-free methods such as weighted/moving least squares [18]. For clarity, let us first assume that no other generalized profile contours exist outside  $\partial\mathcal{O}$ . Denoting the edges of the facets of  $\mathcal{A}_+$  by  $\mathcal{E}_+$ ,  $\partial\mathcal{O}$  is constructed by the following algorithm:

1. Construct the set  $\mathcal{F}_0 \subset \mathcal{E}_+$  of the edges of  $\mathcal{E}_+$  that are shared by a facet in  $\mathcal{A}_+$  and by a facet not in  $\mathcal{A}_+$  but for which  $\langle \nu, \omega \rangle \geq 0$ .
2. Construct the set  $\mathcal{F} \subset \mathcal{E}_+$  of the edges shared by a facet of  $\mathcal{A}_+$  and a facet for which  $\langle \nu, \omega \rangle < 0$ .
3. Construct the connected and ordered line sequences (lists of vertices)  $\Sigma_{0i}$  of the adjacent edges of  $\mathcal{F}_0$ . The edges are defined by two vertices, and within  $\Sigma_{0i}$  one vertex shares two edges.
4. Construct the connected sequences  $\Sigma_i$  from  $\mathcal{F}$  as in 3.
5. The projections of the line sequences  $\mathcal{P}(\omega, \Sigma_{0i})$  cannot intersect each other, but  $\mathcal{P}(\omega, \Sigma_i)$  can intersect each other and  $\mathcal{P}(\omega, \Sigma_{0i})$  (intersection of projections can only occur when the surface folds away from sight, i.e., the line corresponds to a facet for which  $\langle \nu, \omega \rangle < 0$ ). For any intersecting projected sequences, find the intersection points  $p_{ij}$  on the projection plane with the intersection test above.

6. Define the visible projections  $\tilde{\Sigma}_{0i}$  and  $\tilde{\Sigma}_i$  as the projected sequences  $\mathcal{P}(\omega, \Sigma_{0i})$  and  $\mathcal{P}(\omega, \Sigma_i)$  that may have a  $p_{ij}$  as an end point.

7. Connect all  $\tilde{\Sigma}_{0i}$  and  $\tilde{\Sigma}_i$  that can form closed circuits (by systematically comparing the endpoints of the sequences). The circuit enclosing all the others (e.g., those due to shadows) is the approximation of the outer profile contour  $\partial\mathcal{O}$ .

If there are more than one generalized profile contours, the identification of the circuits should be arranged suitably to enable the comparison between the model and the data. For example, one shadow region inside  $\partial\mathcal{O}$  and a smaller  $\partial\mathcal{O}_2$  outside  $\partial\mathcal{O}$  due to a separate closed surface can be identified directly, and all circuits can be used in determining the best model.

The position of a point in  $\partial\mathcal{O}$  can be parametrized by using the path length along  $\partial\mathcal{O}$ . The  $\chi_{\partial}^2$  is now given by (assuming one contour per profile)

$$\chi_{\partial}^2 = \sum_{ij} \|\varkappa_o(c_{ij}) - (\varkappa_m(c_{i0} + c_{ij}) - \varkappa_{i0})\|^2 + \lambda \sum_i (S_i - C_i)^2, \quad (19)$$

where o an m stand for observed and modelled,  $0 \leq c \leq 1$  is the normalized path length along the measured and modelled contours  $\partial\mathcal{M}_i$ ,  $\partial\mathcal{O}_i$ ,  $\varkappa_{i0}$  is the profile offset for each profile  $i$ ,  $c_{i0}$  is the offset parameter for the path's starting point,  $\lambda$  is a suitable weight factor, and

$$S_i = \oint_{\partial\mathcal{M}_i} ds, \quad C_i = \oint_{\partial\mathcal{O}_i} ds. \quad (20)$$

Thus,  $c = s/S_i$  or  $c = s/C_i$ , where  $s$  is the usual path length.

The contour fit can also be modelled by considering the distances of observed points from the model contour  $\partial\mathcal{O}$ . Now we define

$$\chi_{\partial}^2 = \sum_{ij} \inf_s \left\{ \|\partial\mathcal{O}_i(s) - \varkappa_{ij}\|^2 \right\}, \quad (21)$$

where  $\varkappa_{ij}$  are the data points, and we label the points on  $\partial\mathcal{O}_i$  by  $s$ , and assume the translation due to  $\varkappa_{i0}$  to be included in  $\partial\mathcal{O}_i(s)$ ; here it suffices to consider points in  $\partial\mathcal{O}$  on whose normal lines  $\varkappa_{ij}$  lies. When  $\partial\mathcal{O}$  is a set of line segments, the shortest distance required in (21) (let us denote it by  $\delta_{\min}$ ) is defined by:

1. Let  $p'_j \in \mathbb{R}^2$  be the projection of  $\varkappa$  on the line coinciding with the  $j$ th line segment (corresponding to  $\tan \alpha = (\xi_a - \xi_b)/(\eta_a - \eta_b)$  and  $(\xi_0, \eta_0) \rightarrow (x, y)$  in the intersection test above):

$$p'_{(1)} = \frac{D^2\xi - CD\eta + CF}{C^2 + D^2}, \quad p'_{(2)} = \frac{C^2\eta - CD\xi + DF}{C^2 + D^2}. \quad (22)$$

If the projection is inside the segment, let  $d'_j$  be the distance between  $p'_j$  and  $\varkappa$ .

2. Let  $d_k$  be the distance of  $\varkappa$  from the  $k$ th end point of the line segments of  $\partial\mathcal{O}$ .

3.  $\delta_{\min}$  is the smallest one of all the distances  $d'_j$  and  $d_k$ .

In addition to solving for the shape, we usually need to determine the target's spin state as well in order to have correct projection directions [12]. In most cases, the target revolves around a constant pole direction  $(\beta, \lambda) \in S^2$  at a constant rotation speed. The profile plane coordinates  $(\xi, \eta)$  are the  $x'_2$ - and  $x'_3$ -components of

$$x' = \mathbf{R} x, \quad (23)$$

where

$$\mathbf{R} = \mathbf{R}_y(\vartheta - \frac{\pi}{2}) \mathbf{R}_z(\psi - \lambda) \mathbf{R}_y(-\beta) \mathbf{R}_z(-\phi_0 - \Omega(t - t_0)), \quad (24)$$

where  $t$  is the time,  $\Omega$  is the rotation speed ( $2\pi/P$  for a constant rotation period  $P$ ),  $\phi_0$  and the epoch  $t_0$  are some initial values, and  $(\vartheta, \psi) \in S^2$  is the direction from the target to the observer. We determine  $(\beta, \lambda)$  and  $\Omega$  when solving the inverse problem. It is easy to accommodate other spin models such as precession [13] or nonconstant rotation speed [16] in this formalism.



### 3.1 Regularization

The parameters  $P$  describing the target usually have to be (moderately) regularized to prevent unrealistic solutions. One aspect is the smoothness of the body; the larger the target is, the less irregular it is expected to be. For some parts of the surface this is explicitly enforced by the profile data, so the regularization mostly pertains to the parts covered only by lightcurves that contain little information on nonconvex features. In those regions, undulation of the surface should be suppressed (the optimal choice of the suppression weight is discussed in section 4).

For starlike bodies  $\mathcal{B}$ , a simple (computationally  $\chi^2$ -like) measure of global regularity is

$$g_S = \int_{\mathcal{B}} [r - \langle r \rangle]^2 d\sigma, \quad (25)$$

where  $r$  is the radius of the model at the point corresponding to the surface element  $d\sigma$ ; for polytopes, we can simply use  $g_S = \sum_i (r_i - \langle r \rangle)^2$ . For such bodies,  $g_S$  is typically quite efficient when the radius is given by a truncated Laplace series (itself a smoothing agent; see section 5 and [11]) and the regularization weight is low. This is usually the case here as the profile contours already prevent runaway solutions, so  $g_S$  is only needed to polish up the resolution level of shape detail. For higher weights or models with independent (uncorrelated) surface points,  $g_S$  is not suitable as it emphasizes global roundedness more than local smoothness.

A measure concentrating on local smoothness (and more suitable for more complex cases) can be constructed by considering the negative values of the curvature function. For polytopes, a practical discrete version of this is computed by measuring how efficiently the facets not in the convex hull of the polytope can be blocked (from viewing or illumination) by their adjacent facets [11]. Taking into account the size and relative tilt angle of the possible blocker facets adjacent to the facet  $i$ , we can define, e.g., the following measure  $\mathcal{C}$  by summing over the polytope and weighting suitably:

$$\mathcal{C} = \frac{1}{\sum_i A_i} \sum_{ij} A_{ij} (1 - \langle \nu_i, \nu_{ij} \rangle), \quad (26)$$

where  $A_i$  denotes the area of the facet  $i$ , and  $A_{ij}$  the areas of those facets around it that are tilted above its plane [11] (for  $i$  in the convex hull,  $\sum_j A_{ij} = 0$  by definition). In regularization, we minimize  $\mathcal{C}$  (for convex bodies  $\mathcal{C} \equiv 0$ ).

A further smoothing constraint, to be used for non-starlike contours  $\partial\mathcal{O}$  if the observations do not cover the profile densely, is given by augmenting (21) by

$$\lambda \sum_i \frac{1}{C_i} \oint_{\partial\mathcal{O}_i} \inf_{\varkappa \in \{\varkappa_{ij}\}} \left\{ \|\partial\mathcal{O}_i(s) - \varkappa\|^2 \right\} ds, \quad (27)$$

which suppresses irregularity on surface parts not projected near the observed profile points.

A physical constraint for most asteroids is that they are principal-axis rotators: their maximum moment of inertia is aligned with the rotation axis due to energy dissipation caused by the nonzero elasticity of the material of the body [20]. The regularization is defined by the symmetric inertia tensor [8]

$$\mathbf{l} = \begin{pmatrix} P_{22} + P_{33} & -P_{12} & -P_{13} \\ -P_{12} & P_{11} + P_{33} & -P_{23} \\ -P_{13} & -P_{23} & P_{11} + P_{22} \end{pmatrix}, \quad (28)$$

where the inertia products  $P_{ij}$  are

$$P_{ij} = \int_{\mathcal{B}} \rho(x) x_i x_j d^3x, \quad (29)$$

and here we choose constant density  $\rho(x) = 1$ . We want to minimize the angle  $\tau$  between the  $z$ -axis of the model and the eigenvector  $I \in \mathbb{R}^3$  (normalized  $\langle I, I \rangle = 1$ ) corresponding to the largest eigenvalue of the inertia matrix  $\mathbf{l}$  of the model shape  $\mathcal{B}$ , so we can choose, for example:

$$g_I = (1 - \cos^2 \tau)^2 = [1 - I_3(\mathcal{B})^2]^2, \quad (30)$$

where the square form  $I_3^2$  is useful for weighting purposes and for removing the sign ambiguity in  $I_3$ . A fast way of evaluating  $I_3$  in (30) for any polyhedron is described in [5]. Again, profile data constrain the result so strongly that usually the weight for  $g_I$  is very low and sometimes can be set to zero to obtain, say,  $\tau < 4^\circ$ . Enforcing a  $\tau$  much lower than this is seldom meaningful due to shape resolution level and inhomogeneities in the density.

## 4 Optimal combination of data modes: maximum compatibility estimate

From the statistical viewpoint, when we have two or more data modes, we consider their simultaneous probability distribution of model parameters and observations (augmented by prior or regularization distributions) in determining the posteriori distribution of the model and the corresponding estimates. The essential problem in this combining is inevitably the weighting of distributions. While the data modes share a common set of parameters describing the underlying model to be solved for, the models and modalities of observations may be completely different, and we seldom know a priori exactly how to compare and weigh their significance.

Let us choose as goodness-of-fit measures (from which probability distributions can be constructed) the  $\chi^2$ -functions of  $n$  data modes. Our task is to construct a joint  $\chi_{\text{tot}}$  with well-defined weighting for each data mode:

$$\chi_{\text{tot}}^2(P, D) = \chi_1^2(P, D_1) + \sum_{i=2}^n \lambda_{i-1} \chi_i^2(P, D_i) \quad D = \{D_i, i = 1, \dots, n\} \quad (31)$$

(to which regularization functions  $g(P)$  can be added), where  $D_i$  denotes the data from the source  $i$ , and  $P \in \mathbb{R}^p$  is the set of model parameter values. We assume the  $\chi_i^2$ -space to be nondegenerate, i.e.,

$$\arg \min \chi_i^2(P) \neq \arg \min \chi_j^2(P), \quad i \neq j$$

In two dimensions, denote

$$\begin{aligned} x(\lambda) &:= \{\chi_1^2 | \min \chi_{\text{tot}}^2; \lambda\}, \\ y(\lambda) &:= \{\chi_2^2 | \min \chi_{\text{tot}}^2; \lambda\}. \end{aligned} \quad (32)$$

The curve

$$\mathcal{S}(\lambda) := [\log x(\lambda), \log y(\lambda)] \quad (33)$$

resembles the well-known ‘‘L-curve’’ related to, e.g., Tikhonov regularization [1, 7, 9]. However, here we make no assumptions on the shape of  $\mathcal{S}$ . The curve  $\mathcal{S}$  is a part of the boundary  $\partial\mathcal{R}$  of the region  $\mathcal{R} \in \mathbb{R}^2$  formed by the mapping  $\chi : \mathbb{P} \rightarrow \mathbb{R}^2$  from the parameter space  $\mathbb{P}$  into  $\chi_i^2$ -space:

$$\chi = \{\mathbb{P} \rightarrow (\log \chi_1^2, \log \chi_2^2)\}, \quad \mathcal{R} = \chi(\mathcal{P})$$

where the set  $\mathcal{P}$  includes all the possible values of model parameters (assuming that  $\chi$  is continuous and well-behaved such that a connected  $\mathcal{R}$  and  $\partial\mathcal{R}$  exist). If the possible values of  $\chi_i^2$  are not bounded, the remaining part  $\partial\mathcal{R} \setminus \mathcal{S}$  stretches droplet-like towards  $(\infty, \infty)$ . The parameter  $\lambda$  describes the position on the interesting part  $\mathcal{S} \subset \partial\mathcal{R}$ , and it is up to us to define a criterion for choosing the optimal value of  $\lambda$ .

The logarithm ensures that the shape of  $\mathcal{S}(\lambda)$  is invariant under unit or scale transforms in the  $\chi_i^2$  as they merely translate  $\mathcal{S}$  in the  $(\log \chi_1^2, \log \chi_2^2)$ -plane. It also provides a meaningful metric for the  $\log \chi_i^2$ -space: distances depict the relative difference in  $\chi^2$ -sense, removing the problem of comparing the absolute values of quite different types of  $\chi_i^2$ . The endpoints of  $\mathcal{S}(\lambda)$  are at  $\lambda = 0$  and  $\lambda = \infty$ , i.e., at the values of  $\chi_i^2$  that result from using only one of the data modes in inversion. We can translate the origin of the  $(\log \chi_1^2, \log \chi_2^2)$ -plane to a more natural position by choosing the new coordinate axes to pass through these endpoints. Denote

$$\begin{aligned} \hat{x}_0 &= \log x(\lambda)|_{\lambda=0} = \log \min \chi_1^2 \\ \hat{y}_0 &= \log y(\lambda)|_{\lambda \rightarrow \infty} = \log \min \chi_2^2. \end{aligned} \quad (34)$$

Then the “ideal point”  $(\hat{x}_0, \hat{y}_0)$  is the new origin in the  $(\log x, \log y)$ -plane. A natural choice for an optimal location on  $\mathcal{S}$  is the point closest to  $(\hat{x}_0, \hat{y}_0)$ , i.e., the parameter values  $P_0 \in \mathbb{P}$  such that

$$P_0 = \arg \min \left( [\log \chi_1^2(P) - \hat{x}_0]^2 + [\log \chi_2^2(P) - \hat{y}_0]^2 \right), \quad (35)$$

so we have, with  $\lambda$  as argument,

$$\lambda_0 = \arg \min \left( [\log x(\lambda) - \hat{x}_0]^2 + [\log y(\lambda) - \hat{y}_0]^2 \right). \quad (36)$$

In this approach, neither the numbers of data points in each  $\chi_i^2$  nor the noise levels as such affect the solution for the optimal  $P_0$  as their scaling effects cancel out in each quadratic term.  $P_0$  is thus a pure compatibility estimate describing the best model compromise explaining the datasets of different modes simultaneously.

We call the point  $P_0$  the *maximum compatibility estimate* (MCE), and  $\lambda_0$  the *maximum compatibility weight* (MCW). This corresponds to the maximum likelihood estimate in the case of one data mode, or to the maximum a posteriori estimate as well since we can include regularization functions here. If regularizing is used, the weights for the functions are either determined in a similar manner (see below), or they can be fixed and the regularization terms are absorbed in  $\chi_1^2$  (otherwise  $\mathcal{S} \subset \partial\mathcal{R}$  does not hold).

Another choice, frequently used in the L-curve approach, is to find the  $\lambda$  at which  $\mathcal{S}$  attains its maximum curvature [9, 7], but evaluating this point is less robust than finding  $\lambda_0$ , and (36) is a more natural prescription, requiring no assumptions on the shape of  $\mathcal{S}$ . We make two implicit assumptions here:

1. The solutions  $P_{\partial\mathcal{R}}$  corresponding to points on  $\partial\mathcal{R}$  should be continuous (and one-to-one) in  $\mathbb{P}$ -space along  $\partial\mathcal{R}$  at least in the vicinity of the solution corresponding to  $\lambda_0$ . If this is not true (in practice, if  $P_\lambda = \arg \min \chi_{\text{tot}}^2(P)$  makes large jumps in  $\mathbb{P}$  for various  $\lambda$  around  $\lambda_0$ ), one should be cautious about the uniqueness and stability of the chosen solution  $P_0$ , and restrict the regions of  $\mathbb{P}$  included in the analysis.
2. The optimal point  $\lambda_0$  on  $\mathcal{S}$  should be feasible: if we have upper limits  $\epsilon_i$  to acceptable  $\chi_i^2$ , the feasible region  $\mathcal{F}$  is the rectangle  $\bigcap_i \{\log \chi_i^2 \leq \log \epsilon_i\}$ . If  $[\log \chi_1^2(P_0), \log \chi_2^2(P_0)] \notin \mathcal{F}$  and  $\mathcal{F} \cap \mathcal{R} \neq \emptyset$ , we choose the point on the portion  $\mathcal{S} \subset \mathcal{R}$  closest to the one corresponding to  $\lambda_0$  (i.e.,  $\log \chi_i^2 = \log \epsilon_i$  for one  $i$ ). If  $\mathcal{F} \cap \mathcal{R} = \emptyset$ , the data modes do not allow a compatible joint model, so either the model is incorrect for one or both data modes, or one or both  $\epsilon_i$  have been estimated too low (e.g., systematic errors have not been taken into account). Note that model insufficiency should be taken into account in the estimation of  $\epsilon_i$ .

Note that, in the interpretation  $\mathcal{R} = \chi(\mathcal{P})$ ,  $\lambda$ ,  $\chi_{\text{tot}}^2$  and  $\partial\mathcal{R}$  are all in fact superfluous quantities, and we can locate the point estimate MCE  $P_0$  entirely without them with standard optimization procedures (and with no extra computational cost). However, it is useful (though computationally somewhat noisier) to approximate  $\mathcal{S}$  via the minimization of  $\chi_{\text{tot}}^2$  with sample values of  $\lambda$  (see Fig. 1), as in addition to obtaining the MCW  $\lambda_0$  (and hence MCE as well) we can plot  $\mathcal{S}$  to examine the mutual behaviour of the complementary data sources (including the position of the feasibility region  $\mathcal{F}$  w.r.t.  $\mathcal{S}$ ). The solution for  $\lambda_0$  is also needed for constructing distributions based on  $\chi_{\text{tot}}^2$ . Another possibility to examine  $\mathcal{R}$  and  $\partial\mathcal{R}$  is direct adaptive Monte Carlo sampling, but this is computationally slow.

This approach straightforwardly generalizes to  $n$   $\chi^2$ -functions and  $n - 1$  parameters  $\lambda_i$  describing the position on the  $n - 1$ -dimensional boundary surface  $\partial\mathcal{R}$  of an  $n$ -dimensional domain  $\mathcal{R}$ : the MCE is

$$P_0 = \arg \min \sum_{i=1}^n \left[ \log \frac{\chi_i^2(P)}{\chi_{i0}^2} \right]^2, \quad \chi_{i0}^2 := \min \chi_i^2(P), \quad (37)$$

and the MCW is

$$\lambda \in \mathbb{R}^{n-1} : \quad \lambda_0 = \arg \min \sum_{i=1}^n \left[ \log \frac{\hat{\chi}_{i,\text{tot}}^2(\lambda)}{\chi_{i0}^2} \right]^2, \quad \hat{\chi}_{i,\text{tot}}^2(\lambda) := \left\{ \chi_i^2 \mid \min \chi_{\text{tot}}^2; \lambda \right\}. \quad (38)$$

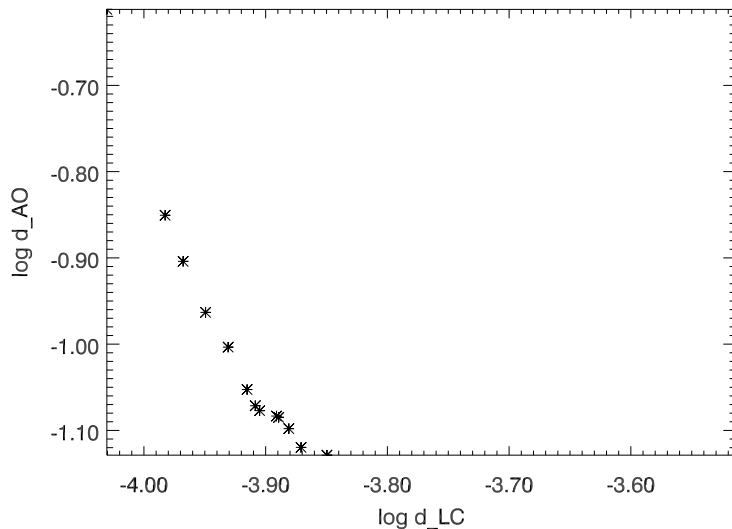


Figure 1:  $\mathcal{S}$  curve plotted for 2 Pallas with various weights  $\lambda$  (LC for lightcurves, AO for adaptive optics profiles).

Another scale invariant version of MCE can be constructed by plotting  $\chi_i^2$  in units of  $\chi_{i0}^2/\chi_{i0}^2$  and shifting the new origin to  $\chi_i^2/\chi_{i0}^2 = 1$ :

$$P_0 = \arg \min \sum_{i=1}^n \left[ \frac{\chi_i^2(P)}{\chi_{i0}^2} - 1 \right]^2, \quad \lambda_0 = \arg \min \sum_{i=1}^n \left[ \frac{\hat{\chi}_{i,\text{tot}}^2(\lambda)}{\chi_{i0}^2} - 1 \right]^2. \quad (39)$$

This, however, is exactly the first-order approximation of (37) and (38) in  $\delta \ll 1$  when  $\chi_i^2/\chi_{i0}^2 = 1 + \delta$ , giving virtually the same result as (37) and (38) as usually  $\chi_i^2(P_0)/\chi_{i0}^2 - 1 \ll 1$  in the region around  $\chi_i^2(P_0)$ , and any larger ratios of  $\chi_i^2/\chi_{i0}^2$  are not eligible for the optimal solution (see Fig. 1).

Instead of the  $L_2$ -norm  $\chi^2$  (and the corresponding  $\chi^2$ -distribution), we can choose some other goodness-of-fit measure  $\varepsilon(P, D) \geq 0$  (and distribution) for the individual data modes. For a linear combination of these, we have

$$\varepsilon_{\text{tot}}(P, D) = \varepsilon_1(P, D_1) + \sum_{i=2}^n \lambda_{i-1} \varepsilon_i(P, D_i).$$

In lightcurve measurements, for example, the effect of systematic errors in both model and data dominates over random noise when the noise level is not high [15], so it is not mandatory to use  $\chi^2$  as a standard measure of fit.

It is possible to use this approach for general regularizing functions  $g(P)$  as well (change  $\chi_i^2 \rightarrow g(P)$  for some  $i$ ), but in such cases the shape of  $\mathcal{S}$  must be taken into account. If it is possible to have a solution  $g(P') = 0$  for a regularizing function  $g$  (or an almost vanishing  $g(P')$  such that  $\log g(P') \rightarrow -\infty$ ), the above scheme automatically returns  $P'$  and ignores the actual data altogether. Thus one should, e.g., set a lower practical limit to  $g(P)$  by looking at the shape of  $\mathcal{S}$ , and choose the  $\lambda_0$  within the restricted part of  $\mathcal{S}$ . Likewise, one can use the above scheme for assigning noise-level-independent weights to subsets of the same data mode (rather than have the standard  $\chi^2$  evaluated from all data points), but obviously the subsets cannot be chosen arbitrarily if the result is to make sense. For example, one can estimate the optimal weight for one lightcurve that appears to reveal features not contained in other lightcurves and thus judge its real significance. Even one noisy lightcurve with a few points, taken at a special observing geometry, may well contain significant information that needs to be weighed more against less noisy but more ordinary lightcurves.

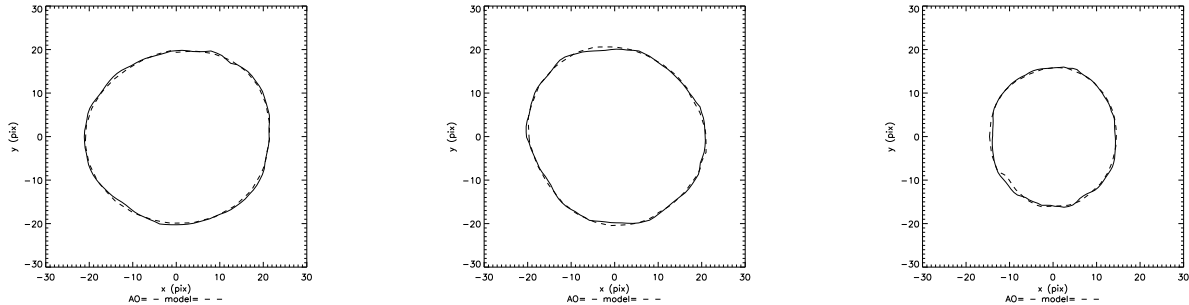


Figure 2: Sample observed (solid lines) vs. modelled (dashed lines) AO contours for 2 Pallas. Coordinates are in pixel units.

## 5 Numerical implementation

As examples of the optimal combining of lightcurves and AO profiles, we show representative results for the asteroids 2 Pallas and 41 Daphne. Full detailed descriptions of the observations and models of these targets are presented in [3] and Carry et al. (in preparation). An example of an even more irregular shape constructed with our procedure is the model of the primary body of the binary asteroid 121 Hermione [4]. The lightcurve  $\chi_L^2$  was computed as in [11, 12] and profile  $\chi_D^2$  as in the starlike case of section 3, and the minimization of  $\chi_{\text{tot}}^2$  was performed as in [11, 12]. The observed profiles are projections of the target on the plane-of-sky  $S^2$  converted to pixels on the instrument plane, while the model is constructed in absolute (km) size, so the model/profile scale conversion is given by the AO instrument’s angular resolution and the distance between the target and the observer. The profile contour extraction procedure with wavelets (as an average of several AO images obtained in a short time interval) is described in [2, 3].

In general, the resolution of the model must be somewhat lower than the apparent resolution of the AO images as the sparse profile samples will produce artificial features elsewhere in the model if a near-perfect profile fit is enforced (even if the observed profile details were exactly right). The inverse problem has thus some ill-posedness at local scales starting near the profile resolution level, but the ill-posedness at more global scales, inherent to lightcurve data [12, 14, 15], is removed with AO profiles. The weight factor  $\lambda$  mostly takes care of this, and fine-tuning is obtained with  $\lambda_S$  for the smoothness constraint  $g_S$ . For the examples here, the weight of the inertia regularization function  $g_I$  was low as there were several profiles available; virtually the same result was achieved with  $\lambda_I = 0$ . The weights  $\lambda$  and  $\lambda_S$  were determined with the scheme of section 4; the examined interval of  $\lambda_S$  was restricted to realistic values corresponding to the resolution level of the AO images.

Fig. 1 depicts a typical evaluation of the curve  $\mathcal{S}$  at various choices of  $\lambda$ ; or rather, this plot portrays the cross-section of the 2-surface  $\partial\mathcal{R}$  in  $\mathbb{R}^3$  with  $\lambda_S$  fixed at its final optimal value. The values for  $\chi_i^2$  are normalized to be the rms deviations of model fits  $d_i = \sqrt{\chi_i^2/N_i}$ , as in logarithmic scale this corresponds only to a shift of origin and a uniform linear change of plot scaling. The plotted points outline the curve  $\mathcal{S}(\lambda)$  that is rather an oblique line than an L-shape, and the ideal point region, i.e., the point closest to the lower left-hand corner, can directly be found. The endpoints  $\lambda = 0$  and  $\lambda = \infty$  stop at saturation regions rather than continue to large distances in the  $\log \chi^2$ -space. As can be seen from Fig. 1, computational noise in the estimated points at  $\lambda = 0$  and  $\lambda = \infty$ , corresponding to a small change of the position of the new origin w.r.t.  $\mathcal{S}$ , does not affect the estimated location of the optimal point on  $\mathcal{S}$  significantly.

Sample observed vs. modelled profiles for 2 Pallas and 41 Daphne are shown in Figs. 2 and 3. The starlike surface model was described by the exponential Laplace (spherical harmonics) series for the surface radius  $r$  [11]

$$r(\theta, \varphi) = \exp \left[ \sum_{lm} c_{lm} Y_l^m(\theta, \varphi) \right], \quad (\theta, \varphi) \in S^2, \quad (40)$$

truncated at suitable  $l, m$ , with  $c_{lm}$  as the shape parameters to be solved for. Other model parameters are

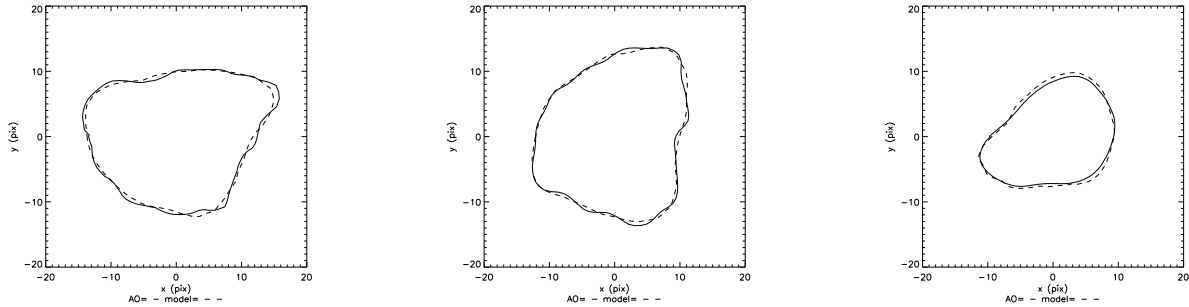


Figure 3: Sample observed (solid lines) vs. modelled (dashed lines) AO contours for 41 Daphne. Coordinates are in pixel units.

the profile offset  $(\xi_0, \eta_0)$  for each image and the spin parameters. For asteroid 2 Pallas (a rather spherical body with size class 500 km), the Laplace series was truncated at maximal  $l = 6, m = 6$ , while for the more irregular 41 Daphne (size class 200 km) the truncation point  $l = 8, m = 6$  was more appropriate. The early truncated Laplace series and the choice of the truncation point are implicit regularization measures as such. We leave the discussion of the choice of model discretization level elsewhere (cf. [17]) as here its effect on the data mode weighting was negligible (within a feasible set of choices), and the resolution level of AO images (as well as keeping  $\lambda_S$  low and avoiding artificial surface features) essentially determined the choice in practice after some sampling. For AO data, the choice of the Laplace series as a model is practical, while for, e.g., detailed space probe data a mesh of independent surface points is more accurate and computationally feasible.

Once the weight factors  $\lambda$  and  $\lambda_S$  are determined, the result is usually stable and restricted to one region in the parameter space  $\mathbb{P}$ : probing feasible solutions  $P$  corresponding to  $\chi_{\text{tot}}^2(P)$  slightly lower than  $\chi_{\text{tot}}^2(P_0)$  produces essentially the same results. Due to restricted orbital geometries, lightcurve data alone often imply two almost equally possible pole directions with mirror-like shape solutions [14, 15]; even one AO (or other) image usually resolves this typical ambiguity [19]. The result is also typically stable w.r.t. weights in the vicinity of MCW. The obtained MCE appears to be well justified when one samples the solutions along  $\mathcal{S}$ : it provides a very good match to profile details without straying far from the observed lightcurves, and does not predict too prominent features on the parts of the surface not projected onto the profile contours.

## 6 Conclusions and discussion

We have examined the classes of shapes reconstructable by the (generalized) profiles of objects in  $\mathbb{R}^3$ , and presented a method for using lightcurves and the observed contours of generalized profiles simultaneously to produce shape (and spin) models with more details (and a lower degree of ill-posedness) than in the pure lightcurve mode. We have also shown that there is a well-justified criterion and an efficient method for determining the optimal weighting of data modes. Applied to real data, the method works very well, and we can use simple regularization functions. In addition to adaptive optics observations, asteroid profiles can also be obtained from other sources such as interferometry, space telescopes, and stellar occultations (partial profiles).

The use of profiles is practical as it removes two sources of systematic errors inherent to using full images (brightness distributions  $\mathcal{I}$  on the image plane): the errors in  $\mathcal{I}$  from AO deconvolution and the model  $\mathcal{I}$  errors due to the insufficiently modellable light-scattering properties of the surface of the target body. On the other hand, profile determination requires the data to be sharp enough, not with fuzzy images. If the images are fuzzy, we usually have to resort to using some brightness and blurring model for fitting full images, even though the result will be less certain.

The concept of the maximum compatibility estimate is directly applicable to any inverse problems with complementary data modes. The invariance properties of the MCE make it more generally usable than heuristic strategies for choosing the weights, especially when they use assumptions on the shape of  $\partial\mathcal{R}$  or other case-specific characteristics.

## Acknowledgements

It is a pleasure to thank Benoit Carry and Josef Āurech for discussions and comments. The sample adaptive optics data used in figures here are courtesy of B. Carry, A. Conrad, J. Drummond, C. Dumas, S. Erard, and W. Merline. This work was supported by the Academy of Finland (project “New mathematical methods in planetary and galactic research”).

## References

- [1] M. Belge, M. Kilmer, and E. Miller, *Efficient determination of multiple regularization parameters in a generalized L-curve framework*, *Inverse Problems*, **18** (2002), 1161-1183.
- [2] B. Carry, C. Dumas, M. Fulchignoni, W. Merline, J. Berthier, D. Hestroffer, T. Fusco, and P. Tamblyn, *Near-infrared mapping and physical properties of the dwarf-planet Ceres*, *Astron. Astrophys.*, **478** (2008), 235-244.
- [3] B. Carry, C. Dumas, M. Kaasalainen, and 9 colleagues, *Physical properties of 2 Pallas*, *Icarus*, (2009) in press.
- [4] P. Descamps and 22 colleagues, *New insights on the binary asteroid 121 Hermione*, *Icarus*, **203** (2009), 88-101.
- [5] A. Dobrovolskis, *Inertia of any polyhedron*, *Icarus*, **124** (1996), 698-704.
- [6] J. Āurech and M. Kaasalainen. *Photometric signatures of highly nonconvex and binary asteroids*, *Astron. Astrophys.*, **404** (2003), 709-714.
- [7] H. Engl and W. Grever, *Using the L-curve for determining optimal regularization parameters*, *Numer. Math.*, **69** (1994), 25-31.
- [8] H. Goldstein, “Classical mechanics” (second edition), Addison-Wesley, Reading, Mass., 1980.
- [9] M. Hanke, *Limitations of the L-curve method in ill-posed problems*, *BIT*, **36** (1996), 287-301.
- [10] M. Kaasalainen, L. Lamberg, K. Lumme, and E. Bowell, *Interpretation of lightcurves of atmosphereless bodies. I. General theory and new inversion schemes*, *Astron. Astrophys.*, **259** (1992), 318-332.
- [11] M. Kaasalainen and J. Torppa, *Optimization methods for asteroid lightcurve inversion. I. Shape determination*, *Icarus*, **153** (2001), 24-36.
- [12] M. Kaasalainen, J. Torppa, and K. Muinonen, *Optimization methods for asteroid lightcurve inversion. II. The complete inverse problem*, *Icarus*, **153** (2001), 37-51.
- [13] M. Kaasalainen, *Interpretation of lightcurves of precessing asteroids*, *Astron. Astrophys.*, **376** (2001), 302-309.
- [14] M. Kaasalainen and L. Lamberg, *Inverse problems of generalized projection operators*, *Inverse Problems* **22** (2006), 749-769.
- [15] M. Kaasalainen and J. Āurech, *Inverse problems of NEO photometry: Imaging the NEO population*, in “Proceedings of IAU: Symposium 236”, **2**, Milani, Valsecchi, and Vokrouhlicky, eds., Cambridge (2007), 151-166.

- [16] M. Kaasalainen, J. Āurech, B. Warner, Y. Krugly, and N. Gaftonyuk, *Acceleration of the rotation of asteroid 1862 Apollo by radiation torques*, Nature, **446** (2007), 420-422.
- [17] J. Kaipio and E. Somersalo, “Statistical and computational inverse problems”, Springer, New York 2005.
- [18] D. Levin, *The approximation power of moving least squares*, Math. Comp., **67** (1998), 1517-1531.
- [19] F. Marchis, M. Kaasalainen, E. Hom, J. Berthier, J. Enriquez, D. Hestroffer, D. Le Mignant, and I. de Pater, *Shape, size and multiplicity of main-belt asteroids. I. Keck adaptive optics survey*, Icarus, **185** (2006), 39-63.
- [20] P. Pravec, A. Harris, and T. Michalowski. *Asteroid rotations*, in “Asteroids III”, Bottke, Cellino, Paolicchi, and Binzel, eds., U. Arizona Press, Tucson (2002), 113-122.
- [21] S. Savarese, M. Andretto, H. Rushmeier, F. Bernardini, and P. Perona, *3D Reconstruction by Shadow Carving: Theory and Practical Evaluation*, International Journal of Computer Vision, **71** (2007), 305-336.

*E-mail address:* First.Lastname [at] tut.fi